Plasmon-Assisted Operando Self-Healing of Cu2O Photocathodes

Plasmon-assisted *operando* self-healing of Cu_2O photocathodes

Aaron Michael Ross,[1] Debora Ruiz-Martinez,[2] Gian Andrea Rizzi,[3] Francesco Cianciaruso,[3] Alessandro Patelli,[4] Marco Salerno,[5] Fabian Schmitz,[6] Enrico Napolitani,[4] Sergio Marras,[5] Mirko Prato,[5] Silvia Gross,[3,7,8] Gaudenzio Meneghesso,[7,9] Rebeca Marcilla,[2] Francesco Scotognella,[1] Teresa Gatti,[6,10*] Francesco Lamberti[3,7*]

[1] Department of Physics, Politecnico di Milano, Piazza Leonardo da Vinci 32, 20133 Milano, Italy
[2] Electrochemical Processes Unit, IMDEA Energy, Avenida Ramón de la Sagra 3, 28935 Móstoles, Madrid, Spain
[3] Department of Chemical Sciences, University of Padova, via Marzolo 1, 35131 Padova, Italy
[4] Department of Physics and Astronomy, University of Padova, via Marzolo 8, 35131 Padova, Italy
[5] Materials Characterization Facility, Istituto Italiano di Tecnologia, Via Morego 30, 16163, Genova, Italy
[6] Center for Materials Research, Justus Liebig University, Heinrich-Buff-Ring 17, 35392 Giessen, Germany
[7] Centro Interdipartimentale Levi Cases, via Marzolo 8, 35131 Padova, Italy
[8] Karlsruher Institut für Technologie (KIT), Institut für Technische Chemie und Polymerchemie (ITCP), Engesserstr. 20, 76131 Karlsruhe, Germany
[9] Department of Information Engineering, University of Padova, Via Gradenigo 6/B, 35131 Padova, Italy
[10] Department of Applied Science and Technology, Politecnico di Torino, C.so Duca degli Abruzzi 24, 10129 Torino, Italy

*Email: francesco.lamberti@unipd.it; teresa.gatti@polito.it

Abstract

The ongoing problems in western countries connected to the global energy supply urgently forces the research community to strive in finding new methodologies for boosting the functional properties of earth-abundant raw materials, for example the largely available cupreous oxide. In this work, we focus on the surface sensitization of this metal oxide semiconductor with an argon plasma treatment, that promotes, during photoelectrochemical hydrogen evolution, the formation of metallic copper nanostructures. Interestingly, these copper-based hierarchical nano-branches, having inherent plasmonic properties, are at the origin of the improved shelf-life of the modified Cu_2O photocathode, as we demonstrate by advanced structural and photophysical analyses. Our proposed photophysical mechanism for an *operando* electrode stabilization suggests that a self-healing process can occur within the Cu_2O/plasmonic Cu heterostructure. These findings pave the way to the implementation of new, easy-to-make strategies to improve the properties of low-cost, low-toxicity energy materials.

Keywords
Copper oxide photocathode, argon plasma treatment, photoelectrochemical water splitting, plasmon assisted photoelectrochemistry, ultra-fast spectroscopy, operando self-healing

Introduction

Cuprous oxide (Cu_2O) is one of the most interesting p-type metal oxide semiconductors, suitable to act as active material for photocathodes in photoelectrochemical (PEC) hydrogen production from water splitting.[1,2] This interest mostly derives from its electronic properties: a suitable band gap for visible light absorption (2.2-2.4 eV) and band positions allowing both hydrogen (HER) and oxygen evolution reaction (OER), the former being the most pursued one.[3] In addition, there is also a relevant economical motivation for deepening our knowledge about this material. For Western economy, Cu_2O can represent an important resource: whereas it shows a relatively large abundance on the Earth´s crust,[4] some EU countries in particular (such as Italy and France), the United Kingdom and Arizona in USA[5] are valuable locations for extensive mining of its mineral form. Furthermore, copper is overall recognized as a non-toxic and non-critical raw material.[4] As witnessed by recent studies, the global request for copper is expected to rise, whereas the world demand will increase by 2–3% per year until 2050.[6] Particularly for an energy-related application such as PEC, this trend will likely be dominant in Europe, where an energy crisis, recently accelerated by the Ukraine war, is currently forcing Germany to reopen coal power plant, Italy to sign new contracts with Algerian oil companies and France to increase investments in nuclear power plants.

Although great expectations are placed on Cu_2O as a sustainable material platform to drive the scale up of hydrogen PEC production, this oxide displays an inherent issue that slows down its entrance into commercial light-driven water electrolyzers, i.e. the poor stability in aqueous solutions. This is due to the fact that the position of the redox potential for protons reduction and the oxidation of monovalent to divalent copper oxide (CuO) lies within the semiconductor bandgap.[7] To overcome this bottleneck, scientists have developed several strategies to preserve the Cu_2O integrity, by stabilizing the surface through deposition of conformal coatings or employing passivating agents.[1] Several examples of these approaches are present in the literature, and here we only mention a few of them. Firstly, we recall the pioneering work of Thimsen and coworkers, in which atomic layer deposition (ALD) was employed to deposit ultrathin layers of titania, zinc oxide and alumina on electrodeposited Cu_2O, achieving up to 7.6 mA cm^{-2} photocurrent under AM 1.5 illumination at a potential of 0 V versus the reversible hydrogen electrode at mild pH.[7] In a more recent work, Grätzel and coworkers have obtained a notable current of 10 mA cm^{-2} using a complex architecture composed of Cu_2O, Ga_2O_3, TiO_2 and RuO_x as PEC catalyst.[8]

In this context, simpler approaches than multilayers oxide structures for boosting the performance of Cu_2O-based PEC devices are required. Argon plasma is commonly used to provide a hydrophilic character to metallic surfaces, improving adhesion between ancillary layers during thin films processing. Furthermore, plasma treatment promotes the formation of nanostructures on surfaces of different materials (polymers[9], copper indium gallium selenide[10], lead sulphide[11], halide perovskites[12]) for several applications. In particular, when treating with Argon plasma the surface of metallic or metal containing films, nanocrystals (NCs) with plasmonic features due to the localized surface plasmon resonance (LSPR) can be generated, paving the way to the integration of plasmonic properties within the treated scaffolds.[13,14] In this regard, one interesting perspective is the exploitation of plasmon-assisted PEC or photocatalysis, which has recently attracted increasing interest due to the ability to efficiently harvest and convert light-energy into highly energetic charge carriers and heat.[15–18]

The general idea of a plasmonic photocurrent is twofold. On one side, the addition of metal nanoparticles that support LSPR can lead to absorption of parts of the solar spectrum not absorbed by the substrate material, and this is analogous to the dye-sensitization of TiO_2 in dye sensitized solar cells (DSSCs). On the other side, the presence of metal nanoparticles that act as “electrons sinks” may allow a more efficient charge separation and therefore an enhancement in the charge transfer efficiency.[19–21]

The use of nanostructuring the components of photoelectrodes for improving the catalytic activity of Cu_2O is not new in the field[22]: for example, in a recent paper nano gold is used for boosting the photocatalytic activity and stability of Cu_2O nanocubes[23], or Xu and coworkers[24] modified a glassy carbon electrode with a composite made of Cu_2O and copper nanoparticles showing improved sensing capabilities. Also the copper/copper oxide matrix can be used for improving photocatalytic response of other metals: in a recent work[25] the nanoparticle Ni activity is boosted by the presence of a Cu/Cu_2O foam. Furthermore, there are several works in which metallic copper LSPR is exploited as sensitizing system as described early[26–29]: for example, Cheng et al.[30] decorate Cu_2O microsphere with copper nanoparticles for boosting the degradation of organic pollutant: in this paper, they support the outcome with the presence of copper LSPR, acting for triggering the visible light absorption. However, in all these papers the copper plasmonic feature has not been realized by a plasma-mediated process, that is trivially simpler to carry on and easier to scale up.

Therefore, in this work, we apply for the first time, to the best of our knowledge, an Argon plasma treatment on Cu_2O electrodeposited thin films, allowing improved performance and durability of this type of photocathodes in PEC HER. Through the combination of a structural and advanced spectroscopic characterization, we attribute these boosted properties to the presence of a nanostructured plasmonic copper layer, whose formation is promoted by the initial Argon plasma treatment and subsequent reduction of Cu(I) to metallic Cu, during PEC activity. This overall picture allows us to suggest a mechanism occurring within the thus-formed Schottky barrier between plasmonic Cu nanostructures and Cu_2O, in which the photo-generated charges contribute to an *operando* self-healing of the photocathode, increasing its functional durability.

Experimental Section

Materials and methods.

All chemicals and solvents were purchased from Merck and used without any further purification.

Cu_2O thin films fabrication, Ar plasma treatment and PEC measurements

Cu_2O thin films were grown by electrochemical deposition in a three electrodes system (Autolab PGSTAT101, Methohm, The Netherlands), using a procedure previously reported in the literature.[31] The working electrode is a Fluorine Tin Oxide (FTO) glass, the counter electrode is a platinum wire and the reference is a saturated calomel electrode (SCE). An aqueous solution of 0.3 M $CuSO_4$ and 4 M lactic acid was prepared and the pH was adjusted by adding a 4 M sodium hydroxide solution, to obtain a final value close to 8.3. The electrochemical bath was maintained at a temperature of about 60°C. Prior to the deposition, a linear sweep voltammetry (LSV) was performed in order to obtain the right potential of reduction (from Cu(II) to Cu(I))[32] (Fig. S1a). Then, the deposition was performed at the potential of -0.35 V vs. SCE for 900 s (Fig. S1b). The samples were then exposed to Ar plasma treatment (Stylus Plasma Noble, Nadir srl (I)) with the following conditions: RF 27 MHz power 20 W, HF 17kHz voltage 10 kV, Ar flow 6 L/min. The films were displaced on a plotting base at a distance of 5 mm from the plasma. The speed was 100 mm/s, step 0.5 mm, 10 passages.

Electrochemical characterization

The photocurrents of the electrodes were evaluated by LSV, in the potential range between 0 V and -0.8 V vs. SCE, and chopped chronoamperometries (CA, switch on/off period 30 s) were recorded at the potential of -0.5 V vs. SCE. LSV and CA were carried out in a nitrogen-saturated $KHCO_3$ 0.5 M solution at pH 11, using a white LED lamp (1.5 V) as the illumination source and an output power density of 92 mW cm^{-2}. The working area of the electrodes was circular (diameter 6 mm) producing an area of 0.028 cm^2.

CA technique was further used to determine the long-term stability of the pristine and plasma-treated Cu_2O electrodes. Specifically, -0.5 V vs. SCE was applied for one hour and a half in total. During the initial 30 minutes, the experiments were conducted using chopped light every 30 s, which means, 30 s under dark (light off) followed by 30 s under illumination. Afterwards, the potential of the electrodes was stabilized by keeping them in dark for around 10 minutes. After this period, the electrodes were illuminated using visible light for 35 minutes and, finally, the light was switched off up to reach 90 minutes. The geometrical area of the electrode was 1 cm^2.

Photocathodes structural characterization

Scanning electron microscopy (SEM) was carried out with a Zeiss Sigma HD microscope, equipped with a Schottky FEG source, one detector for backscattered electrons and two detectors for secondary electrons (InLens and Everhart Thornley). The microscope is coupled to an energy-dispersive X-ray (EDX) detector (x-act PentaFET Precision, Oxford Instruments) for X-rays microanalysis, working in energy-dispersive mode. In order to improve the spatial resolution of X-ray microanalysis and to reduce the absorption of low energy photons due to the FTO substrate, a low beam energy (3 KeV) was used. The estimated range of X-ray production for O k-shell and Cu L-shell in a Cu_2O matrix of density 6 g/cm^3 matrix are 68 nm and 77 nm, respectively, as described by the Kanaya–Okayama (1974) equation modified for the threshold of X-ray production[33].

Dynamic secondary ion mass spectrometry (SIMS) measurements were carried out with a Cameca IMS-4f spectrometer, using a Cs^+ primary beam while collecting $^{133}Cs^{16}O^+$ and $^{133}Cs^{63}Cu^+$ secondary ions. The depth scale has been calibrated by measuring the crater depth with a Tencor P-17 profilometer and assuming a uniform sputter rate.

X-ray diffraction (XRD) patterns were recorded on a Malvern-PANalytical 3rd generation Empyrean X-ray diffractometer, equipped with a 1.8 kW CuKα ceramic X-ray tube and PIXcel3D detector, operating at 45 kV and 40 mA in 1D mode. The diffraction patterns were collected in air at room temperature, using Bragg-Brentano (BB) geometry. XRD data analysis was carried out using HighScore 5.1 software from PANalytical.

Kelvin probe characterization

The samples were measured with an atomic force microscope (AFM) MFP-3D by Asylum Research (Oxford Instruments), operating in ambient air as a scanning Kelvin probe microscope (SKPM) in double-pass mode, at a typical elevation of 50 nm. The electrically conductive probe was a RTESPA-300 (Bruker), consisting of monolithic silicon, highly-doped with N (i.e. n-type), resulting in resistivity as low as 0.01-0.25 Ωcm, with nominal central values of spring constant, resonance frequency and tip apex radius of curvature of 40 N/m, 300 kHz, and 10 nm, respectively. The probe was calibrated against highly-oriented pyrolytic graphite (HOPG), assumed to exhibit a work function of 4.60 eV. The measurements (20 µm scan size, 0.5 Hz scan line frequency, 256x256 pixels) were repeated in three different locations on the sample surface, and always showed uniform surfaces with grainy appearance, result in consistent values of electric surface potential within the experimental error, which can be estimated to be around ±50 mV.

Linear absorption and micro transmission contrast

Linear absorption measurements were carried out with a Jasco V-570 spectrophotometer. Micro-transmission contrast experiments were carried out with the white light probe (WL) used in the transient absorption experiments described below. The WL spectrum spanned from 420-700 nm and was focused to a 260 µm effective diameter spot on the sample, recollimated in transmission and dispersed on a grating spectrometer equipped with a Si optical multichannel analyzer (Stresing Entwicklungsbüro). Transmission contrast, defined here as

$$T_{contrast} = \frac{T_{WL} - T_{sample}}{T_{WL}}$$

was determined by measuring the transmitted probe spectrum through the sample T_{sample}, and then removing the sample and measuring the spectrum T_{WL}. Larger values of $T_{contrast}$ correspond to higher sample absorption.

Ultrafast transient absorption spectroscopy

Ultrafast pulses were generated with a Ti:Sapphire chirped pulse amplified laser (Coherent Libra) with 2 kHz repetition rate, a central wavelength of 800 nm, and a pulse FWHM duration of 100 fs. The fundamental pulse was split between a pump and probe path. In the pump path, second-harmonic generation was carried out in a beta-barium borate (BBO) crystal resulting in 400 nm pump pulses; the fundamental wavelength at 800 nm was spectrally filtered out with BG39 Schott glass filters. The pump was mechanically chopped at 1 kHz and delayed via a mechanical delay line out to 1 ns pump-probe delay. The pump was orthogonally linearly polarized to the probe and focused down to a 480 µm diameter spot at the sample location, as well as polarization-filtered with a polarization analyzer before the spectrometer slit. On the probe path, the 800 nm beam was spatially filtered with an iris, attenuated, and focused into a sapphire window for white light generation (WLG), and re-collimated by a reflective spherical mirror. The probe was focused onto the sample with < 260 µm effective diameter at a small angle, re-collimated with a lens and sent to the high-speed spectrometer used in micro-transmission contrast. Differential transmission spectra $dT/T = \frac{T_{pumpON} - T_{pumpOFF}}{T_{pumpOFF}}$ were determined by comparing the sample-attenuated dispersed white light probe when the pump interacted with the sample and when it was blocked by the chopper. Measurement and analysis software included Labview and Matlab 2020a. During the analysis, the measured transient absorption (TA) maps were dechirped and the cross-phase modulation (XPM) artifact was removed.

Global analysis

Global analysis of the transient absorption was performed with Matlab 2020a code [Ross2021]. It is assumed that the TA kinetics are described by the sum of a finite number of exponential decays convolved with the Gaussian instrument response function. Each decay is associated with a physical process related to the decay and filling of populations. For a chosen number of exponential decays for a given model, the coefficients (weights) for each decay are optimized in the model fitting procedure as a function of probe wavelength only. The signal can be written as:

$$S(\lambda, \Delta t) = \mathrm{IRF} * \sum_{j=1}^{N} A_j(\lambda) e^{\frac{-\Delta t}{\tau}} \quad (1)$$

where IRF is the instrument response function, which is taken to be a Gaussian function with the FWHM of the pump pulse, and is convolved with the sum of weighted exponential decays with lifetimes τ. Δt is the pump-probe delay, and λ is the probe wavelength. The probe wavelength-dependent coefficients $A_j(\lambda)$ are called decay-associated spectra (DAS) and are reported in the main figures in the paper.

Results and Discussion

The Ar plasma-treated and pristine Cu_2O thin films were characterized for their PEC performance as described in the Experimental Section. The pristine sample was previously characterized with a chopped LSV at negative potentials for a rough estimation of the working potential (Fig. S1c): a typical reductive peak centred at -0.5V (vs. SCE) was found.

Fig. 1a and 1b show the electrochemical behaviour for pristine and plasma-treated Cu_2O, respectively. Fig. 1c and 1d show the details for pristine and plasma-treated Cu_2O electrodes, respectively.

As observed in Fig. 1a and 1b, the plasma treatment enhances both the electro- and the photoelectrochemical operation of the Cu_2O. On the one hand, the current density affords by the plasma-treated electrode in dark is more stable than the one obtained with pristine Cu_2O, which could be related with a chemical and photoelectrochemical corrosion of the electrode without the plasmonic treatment in contact with the electrolyte and the light exposure. On the other hand, the plasma treatment improves the conductivity of the semiconductor and the absorption of visible light, which is denoted by the higher photocurrent achieved in the plasma-treated Cu_2O and also its large instantaneous photocurrent.

Fig. 1c and 1d show the electrochemical behavior for the same pristine and plasma-treated Cu_2O electrodes, respectively, after increasing the light exposure time. As observed in Fig. 1c, the photocurrent provides by the pristine Cu_2O is significantly lower in comparison with the beginning of the CA in Fig. 1a. In fact, the current is continuously decreasing along the experiment which is due to some corrosion of the material during the long-term experiment. Furthermore, there was no significant change in the current for the pristine electrode when the light was switched off after the illumination period (Fig. 1c). On the contrary, the plasma-treated electrode shows an enhanced photoelectrochemical behavior in the long test experiment, keeping a similar photocurrent as at the beginning of the CA in Fig. 1d.

In addition, a prolonged chopped CA for estimating the generated photocurrent was performed (Fig. S1b), where the solid black line refers to the pristine sample, whereas the solid red line refers to the plasma treated one. The potential was kept constant allowing the HER. Across the first 50 min of continuous measurements, the current density of the plasma-treated sample remained always higher than the one of the pristine one, suggesting that the plasma treatment is somehow stabilizing the PEC interface. The best performing plasma-treated photocathode showed a current density of 40 $\mu A/cm^2$ (about 100% better than that of the pristine sample)

Furthermore, it is worth mentioning the good mechanical stability of the plasma-treated electrode after the long CA test. As observed in the inset of Fig. 1d, the film remains stable on the substrate after it, contrary to the observed in the pristine Cu_2O electrode, inset in Fig. 1c.

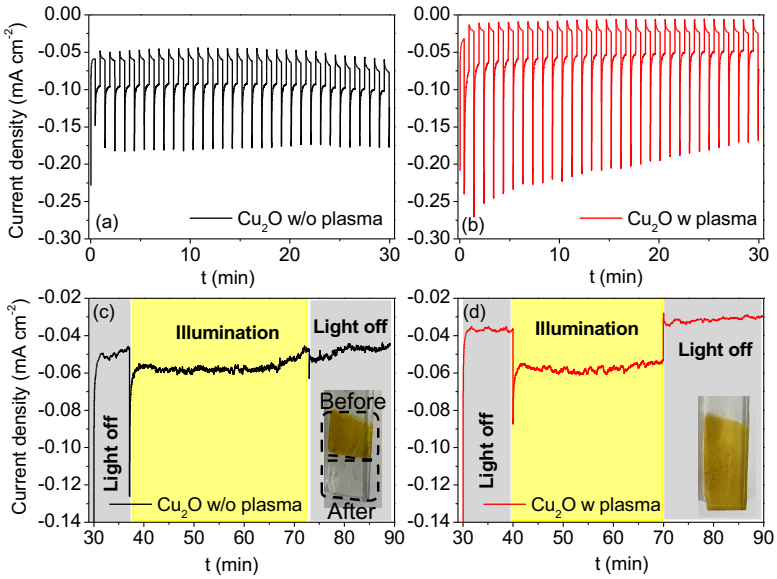

Figure 1. CA at -0.5 V vs. SCE for a (a) and (c) pristine Cu_2O and (b) and (d) plasma-treated Cu_2O. The experiments were performed in a three-electrode photoelectrochemical cell. The electrolyte was degassed bubbling Ar for 15 minutes previous to the electrochemical tests..

In order to get complete information on the literature of copper oxides structures, a comprehensive survey of electrodeposited Cu_2O photocathodes protected by thin layers of different oxides like TiO_2, Al_2O_3, ZnO etc., grown by ALD can be found.[34] The recorded photocurrent densities span from 1.8 mA/cm^2 up to almost 7 mA/cm^2 in the case of AZO/TiO_2 protected Cu_2O.[35] Other interesting examples of protected Cu_2O photocathodes are a g-C_3N_4/Cu_2O heterostructure with photocurrent densities of about 1.5 mA/cm^2 at 0.0 V vs. RHE[36] and the case of Cu_2O/CuO/C heterostructure with a photocurrent density of about 7 mA/cm^2 at 0 V vs. RHE.[37]

With the intention of understanding the effect of the Ar plasma treatment on the performance of Cu_2O thin films, we firstly examined the structural and morphological features of the photocathodes before and after their use for PEC HER.

XRD analysis of samples before PEC analysis (Fig. S2a) reveals the presence of the sole Cu_2O phase, showing no difference between the samples (neither in intensities of reflexes nor in their FWHM), thus confirming that the plasma treatment affects only the first layers of the oxides without modifying the bulk. Furthermore, in Fig. S2b a graph detail, in the range 30°-60°, confirms that no reflexes due to reduced copper-based species (CuO and Cu) are present, allowing us to state that the electrodeposition of a pure Cu_2O phase has occurred.

Detailed morphological characterization is carried out by SEM. In Figure 2, SEM top view and cross section images of the different samples are presented. The Cu_2O surface of a freshly electrodeposited sample looks like a uniform layer composed of grains of 200 nm lateral size (Fig. 2a,c). On the other hand, top view images of the plasma treated samples show a modified surface characterized by the creation of holes (highlighted in the detail in Fig. 2c). This surface restructuring

cannot be created by argon ions physical etching, since their energy is limited by collisions at atmospheric pressure. On the contrary, the nature of the surface change must be sought in the chemistry domain. A noble gas plasma - due to the presence of free electrons - presents a naturally reducing environment. It is important to point out that the plasma-promoted reduction of copper oxides has been already reported in literature[38,39] and the reduction process of CuO is favorable respect to Cu_2O, although both processes can be observed[40]. In addition, the oxide surface is chemically activated during the plasma jet scanning by the creation of hydrophilic hydroxyl groups that favor the moisture absorption speeding up the electroreduction process by hydrogen intercalation. The reduction process induces a surface reorganization letting the clustering of the oxide/metallic phases[41] and the release of molecular oxygen. The new surface, therefore, appear with hills and craters as the surface of a sponge[42]. This morphology is more visible on grain boundaries. The darker appearance of these holes in the SEM image may be due to the presence on not completely reduced oxide species. In addition, in the SEM image the grains appear more defined in the plasma-treated Cu_2O with respect to the pristine one. This visual effect is probably due to the reduced surface charging during the imaging, thanks to the metallic copper, and to specific location of the reduction process. The reduction reaction is in fact enabled by the availability of electrons and hydrogen ions, which is driven respectively by the conductivity and diffusivity both greater right on the surface and in the grain boundaries.

The PEC HER process produces another relevant feature on the metal oxide surface: both samples show the formation of a layer of NCs, which are fused and densely packed in the pristine sample (Fig. 2b), or randomly dispersed and/or combined in little islands in the plasma-treated sample, leaving around many voids (Fig. 2d), with formation of a complex 3D nanostructured architecture. Also, EDX analysis demonstrates that the atomic percentage ratio is almost the same in the samples pre-PEC as in the plasma-treated sample after PEC (about 2.5, thus confirming the stoichiometry of Cu_2O), while the pristine sample after PEC shows a value that is more than double (6.5), suggesting that a consistent amount of metallic copper is now present. This feature has already been observed previously in electrodeposited Cu_2O films that have undergone PEC HER:[43] the presence of copper cuboids nucleated on the surface of the cupreous oxide was highlighted and this is the most direct indication of dissolution of Cu_2O during the process, which brings to the steep decrease in performance of similar photocathodes in their pristine form during continuous operation (Fig. 1, black curve).

From the analysis of these top layers after the PEC measurements in the two types of samples, we have first evidence that the Ar-plasma treatment prevents the metal oxide decomposition to a large extent. What is new and relevant to observe is a nanostructured hierarchical architecture, whose formation is favoured by the preliminary plasma treatment of the Cu_2O surface: in this regard, we speculate that the holes created by the plasma etching act as nucleation centres for the formation of metallic copper NCs. In the untreated sample, where these nucleation seeds are missing, the growth proceeds in all directions, thus forming a fused layer of copper particles that is almost like a homogeneous film. As we will discuss later in the text, this slight difference in the copper-based capping layer conformation strongly affects the optical properties and therefore the stability of the cupreous oxide photocathode.

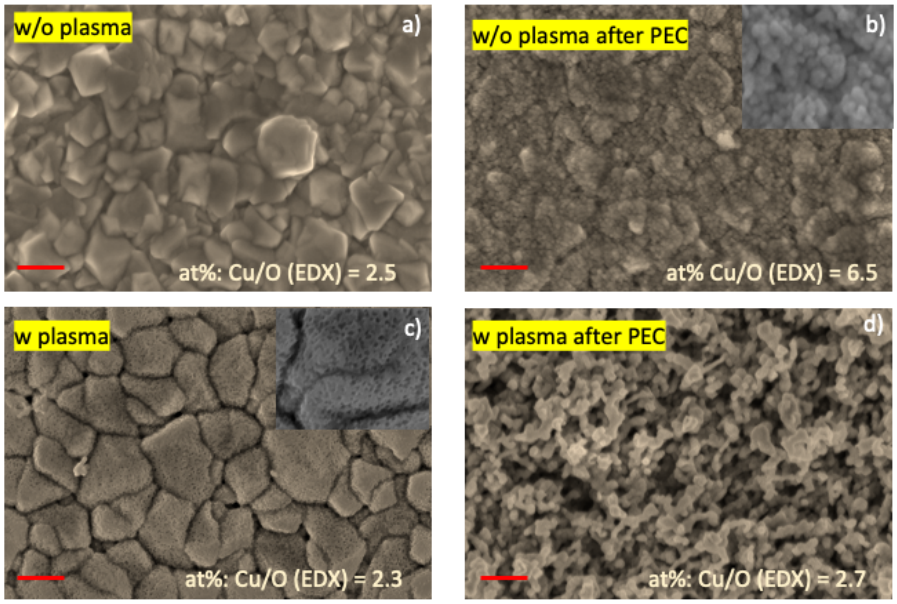

Figure 2. SEM characterization of electrodeposited Cu_2O thin films on FTO with and without Ar-plasma treatment. Top view image of a) pristine and c) plasma treated sample before and b) and d) after PEC HER. Scale bar is 200 nm. The atomic percentage (at%) ratio between copper and oxygen derived from EDX characterization is provided at the bottom right side of each image.

In Fig. 3, cross sectional SEM images of the samples are shown. These images are informative because they provide a lateral view of the thin films and especially allow to examine the metallic copper capping layer formed during the PEC process. In Fig. 3a) and 3c), where the pristine and plasma-treated samples are shown, a dense and packed layer of Cu_2O grown on FTO is visible. The plasma does not affect the bulk of the film, which is roughly 500 nm thick. In Fig. 3b) and 3d), the same films after PEC feature the presence of the copper capping layer. On top of the pristine cupreous oxide, a relatively thin capping layer of copper has formed, in which the NCs are fused to each other, whereas the plasma-treated sample is covered with a rough and nanostructured layer of isolated clustered NCs with a high overall surface, as it was arguable from top-view. In order to investigate the quality of this capping layer, we performed an EDX depth profile of the cross section (Fig. S3): this analysis shows that the amount of copper (in wt%) is notably higher in the top 200 nm of the film, which is indeed the thickness of the formed coating, reasonably constituted mostly of metallic copper.

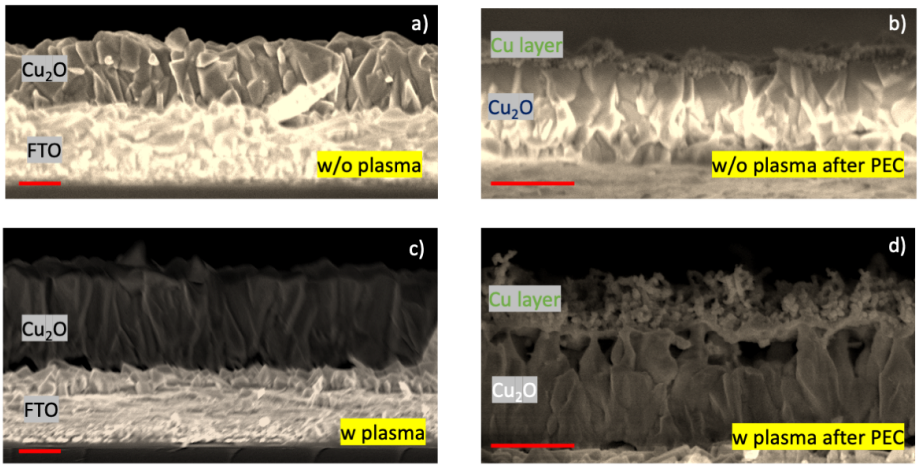

Figure 3. Cross sectional SEM images for pristine electrodeposited Cu_2O thin films pre- a) and post-PEC HER b) and for plasma treated films pre- c) and d) post-PEC HER. Legend bar is 200 nm in each image.

Additionally, in order to obtain a more detailed depth profile of the Cu layer in the plasma treated sample, SIMS analysis was also carried out (Fig. 4a). Both $^{133}Cs^{16}O^+$ and $^{133}Cs^{63}Cu^+$ signals (see Experimental Methods for details) show significant similar fluctuations within the first 0.4 µm below the surface, before stabilizing with a plateau down to the substrate interface, clearly identified by a drop in the $^{133}Cs^{63}Cu^+$ yield. We believe that such fluctuations are related with the structural changes induced by PEC in the upper part of the electrode (supporting SEM analysis), which affect the SIMS sputtering yield. $^{133}Cs^{63}Cu^+/^{133}Cs^{16}O^+$ ratio (solid red line in Fig. 4a) qualitatively suggests that the layer is formed by a shallow region, approximately 0.1 µm thick, which is richer in Cu, followed by two regions with decreasing Cu concentrations, in agreement with the EDX observations.

The morphological characterization as a whole confirms that PEC HER, thus a process happening under reducing conditions, produces a compact metallic copper capping layer (Cu layer) deriving from the dissolution of the Cu_2O structure, whereas the Ar-plasma treatment induces nucleation dynamics for metallic copper (Cu seeds), which causes an anisotropic and hierarchical growth of a metallic NC architecture (Cu branches) with high surface area and roughness, as roughly illustrated in Fig. 4b.

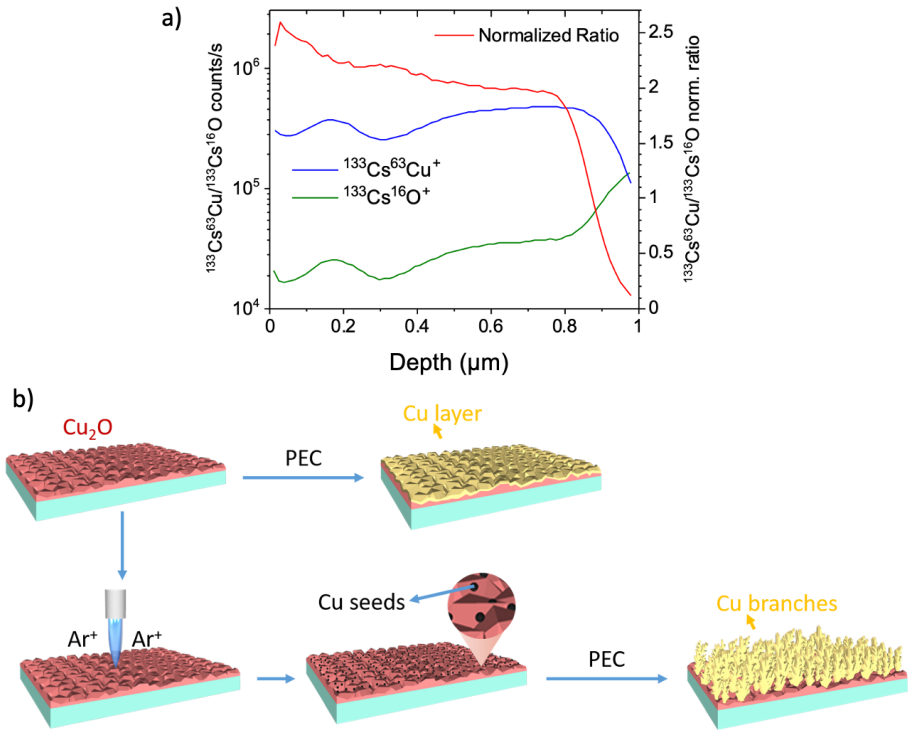

Figure 4. a) SIMS analysis performed on plasma treated Cu_2O sample; b) sketch representing the combined effect of Ar plasma treatment and PEC on different Cu_2O photocathodes.

To further study the effect of the plasma treatment on the PEC properties of Cu_2O photocathodes, an advanced optical analysis was performed, using linear and transient absorption spectroscopy on the different samples. The optical properties of copper oxides, including cuprous oxide or cuprite (Cu_2O) and cupric oxide (CuO), vary significantly from one sample to the next one. These properties, especially the bandgap energies, depend strongly on the synthesis process (radio-frequency magnetron sputtering[44], electrodeposition[43,45], oxidation of Cu in a furnace[46], nanocrystal morphology - nanorods[46], and quantum confinement effects[47]). Reported values of bandgap energies range from 2-2.5 eV for Cu_2O to 1.2-2.16 eV for CuO[43,45,46,48–50]. The photo-physics is further complicated by the presence of excitons at room temperature, which appear in samples annealed at high temperature (930 °C), with binding energies in the range of 46-150 meV[48]. These excitonic energies are expected to range from 2.13 eV (onset of band-to-band absorption) to 2.7 eV[48], and have been shown to play a major role in Cu_2O-based photovoltaic devices[51]. Furthermore, in Cu_2O, the lowest energy interband transition predicted at 2.17 eV is direct but parity-forbidden[48], and a so-called direct optical bandgap is often observed at 2.4 eV or higher energy, in addition to an indirect bandgap that may also appear[46]. These band structure properties are often neglected during the fitting of the Tauc plot used to determine the bandgap, where the fit exponent depends on whether the gap is direct or indirect. It is fundamental to point out that no differences are derived from samples before and after the PEC analysis (i.e. there are not variations

induced by PEC measurements), therefore the unique consistent variations for the photophysical characterization and related discussion are due by the effect of plasma treatment.
The absorption spectra for both pristine and plasma-treated samples are highly inhomogeneous, as can be seen by measuring different spots on the samples (Fig. 5a,b).

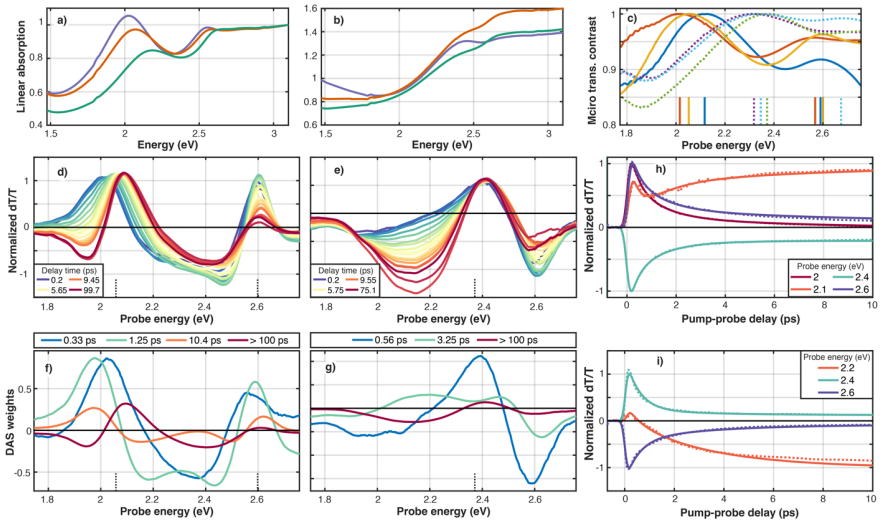

Figure 5. Characterization of opto-physical properties of pristine and plasma-treated Cu_2O thin films. a,b): Linear absorption collected using a spectrophotometer (5 mm spot size) for plasma-treated a) and pristine b) Cu_2O thin films. Different curves are different spots on the sample. c): Micro transmission contrast taken using same white light continuum probe with ~100 µm spot size diameter as in the differential transmission experiments at different spots on the two samples (see Methods section). Solid lines are the plasma-treated sample spectra, dashed lines are the pristine Cu_2O sample spectra, with corresponding peak centers displayed beneath the curves with vertical energy markers. d,e): Differential transmission (dT/T) spectra at pump-probe delay times ranging from -0.2 to 100 ps for plasma-treated d) and pristine e) Cu_2O thin films. f,g): Decay-associated spectra (DAS) results from global fitting analysis (see Table S2), with exponential decay times listed in the legends above each plot for plasma-treated f) and pristine g) Cu_2O thin films. In panels d-f, dashed vertical lines correspond to the energies of linear absorption peaks determined from micro-absorption (see Figure S5). h,i): dT/T dynamics (dashed lines) at selected probe energies for plasma-treated h) and pristine i) Cu_2O thin films with fits resulting from global analysis (solid lines). The pump fluence for TA data was 380 µJ cm^{-2}.

For the plasma-treated Cu_2O samples, while the absorption onset at high energy begins around 2.55 eV, a strong resonance feature appears with peak energies ranging from 2.01 to 2.19 eV (Fig. 5a and 5c, solid lines). We attribute the resonance to the LSPR of Cu NCs that are observed in the SEM images of the plasma-treated samples only (Fig. 2,3). The LSPR energy is in strong agreement with previous measurements of Cu nanoplates[52–57], and the higher inhomogeneity of the LSPR feature relative to the interband absorption of Cu_2O reflects variations in the NC size, morphology, and electron density throughout the sample. We point out that Cu has lower "free electron character" than the more commonly used noble metal Au/Ag plasmonic systems, due to strong variations in both the real and imaginary dielectric function in the visible[52]. Thus, part of the optical response in our sample might also be due to interband absorption of Cu, although the strong absorption strength relative to the interband absorption of Cu_2O provides substantial evidence for the Cu LSPR. We find no evidence from either linear or transient absorption measurements of the presence of Cu NCs in the pristine Cu_2O sample. Significantly, we note that the LSPR resonance remains prominent over time without taking any effort to protect the samples from oxidation.

We performed ultrafast TA experiments on the pristine and plasma-treated Cu_2O thin film samples (Methods section). The samples were pumped at 3.1 eV (400 nm) and the pump-induced change in probe transmission was detected as a function of probe wavelength and pump-probe pulse delay time. The normalized differential transmission (dT/T) spectra are plotted in Fig. 4d,e for both samples. The two plots are qualitatively representative of other spectra taken at different spots on the sample. Additionally, at each spot we measured the micro-transmission contrast, which provides us information about the linear absorption maxima indicated in dashed vertical lines (Fig. 4c-g) while reducing the inhomogeneity sampled by the probe.

In the case of pristine Cu_2O (Fig. 5e), the 3.1 eV pump drives interband transitions in the semiconductor thin film. At early pump-probe times there is a strong bleaching (positive dT/T) signal, centered almost exactly at the absorption maximum around 2.37 eV, as determined from micro-transmission contrast (dashed vertical markers in Fig. 5e and 5c), as well as a negative feature at energies greater than 2.5 eV and lower than 2.2 eV. This lineshape may be explained by the combination of multiple mechanisms: i. The bleaching of excitonic states[48]; ii. The nearly-instantaneous filling of the conduction band (CB) minimum resulting in a bleaching signal, and iii. a so-called Fermi-smearing around the band-edge, which arises from the pump-induced elevation of the carrier temperatures and results in a band-edge shift[58,59]. Within 600 fs (see global analysis section) during the hot carrier thermalization process, the dT/T signal drops significantly, and over 3-4 ps a new pump-induced absorption (PIA) negative dT/T signal appears, between 1.9 and 2.3 eV (Fig. 5i orange curve). This signal corresponds to the in-filling of surface and interfacial states in the Urbach tail observed in linear absorption[60,61]. The dT/T spectra remain effectively constant after 100 ps.

In the other case, for plasma-treated Cu_2O, the transient optical response is quite different. First, the micro-transmission contrast reveals two absorption maxima at 2.6 and 2.05 eV instead of just one as in pristine Cu_2O, which overlap with the two strong features observed in the dT/T spectra (Fig. 5d). The dT/T feature observed at 2.6 eV is similar to the one from pristine Cu_2O, with a strong bleaching centered at the absorption maximum, and negative “wings” on both the red and blue edges of the bleaching feature. Notably, the plasma-treatment results in a blue-shift of the bleaching peak from pristine Cu_2O by at least 0.2 eV. Most significantly, a new strong resonance appears after plasma-treatment centered in the transmission contrast at 2.05 eV, which we attribute to the LSPR of Cu NCs which were identified in SEM (Fig. 3). In the normalized dT/T spectra (Fig.xc 4d), the pump-induced bleaching of the LSPR via interband excitation in both Cu[56] and Cu_2O is relatively strong compared to the band-edge changes. A striking dynamic blue-shift of the LSPR occurs (see global analysis section and mechanisms discussion) as seen by the dynamics at 2.1 eV, which first decays over 600 fs and then rises again over the course of 10-20 ps (Fig. 5h orange curve). One important result is that the bleaching of both the Cu_2O band-edge and Cu NC LSPR occur simultaneously when the pump and probe overlap (time zero), implying a shared photo-physical mechanism. Interband excitation leads to an excitation of free carriers in the CB, thereby modifying the Drude parameters that directly influence the LSPR resonance energy and linewidth[62]. As discussed later, hot carrier transfer effects between Cu_2O and the Cu NCs likely explain the dynamic blue-shift of the LSPR rather than the nearly instantaneous dT/T observed near time-zero.

To further investigate the photo-physical mechanisms underpinning the differences between the pristine and plasma-treated Cu_2O thin film samples, we fit the dT/T spectra and dynamics via global analysis[63] (see Methods and Supplementary Discussion). The dramatic spectral shifts of the feature at 2.05 eV after interband excitation provide substantial evidence that the feature is plasmonic, considering the well-known sensitivity of the LSPR of noble metal plasmonic nanocrystals to changes in both their environment and electronic/lattice systems[64–67].

In the plasma-treated Cu_2O-Cu heterostructure, hot carrier transport effects play a significant role in determining the transient optical properties. The system can be treated as a Schottky diode, or junction, between a doped semiconductor (Cu_2O) and a metal (Cu). An additional complication arises from the fact that the Cu forms NCs during the plasma-treatment process, resulting in the demonstrated strong LSPR resonances. Thus, the metal can be excited directly well below the band-gap, in contrast to a typical Schottky diode structure, which has a metallic region that is either bulk or thin film. Such a heterostructure device, which consists of a semiconductor and plasmonic NCs, can exhibit photo-induced hot carrier transport in both directions[53,68–71].

The band diagram for the Schottky diode along with the relevant photo-physical processes leading to hot carrier transport are shown in Fig. 6. The work functions were measured using Kelvin probe microscopy (Table S1) to be equal to 5.3 eV and 5.5 eV for the plasma-treated and pristine Cu_2O samples, respectively. The work function of Cu was taken to be 4.5 eV[72], the electron affinity of Cu_2O as 3.2 eV[73], and the band-gap of Cu_2O as 2.2-2.4 eV[43,44,54], a value that is consistent with the Tauc plot analysis conducted on pristine Cu_2O samples (Fig. S4), where a band-gap value for pristine Cu_2O was found to be 2.35 eV. Thus, as seen in the band diagram with accurate scaling, Cu_2O is confirmed to be a p-doped semiconductor, and the work function of Cu is slightly below the reversible hydrogen electrode potential[74]. Considering the relevant work functions of the two materials ($\phi_{Cu} < \phi_{Cu2O}$), when the Schottky diode is formed, a barrier is formed to hole transport rather than electron transport across the junction (Fig. 6a).

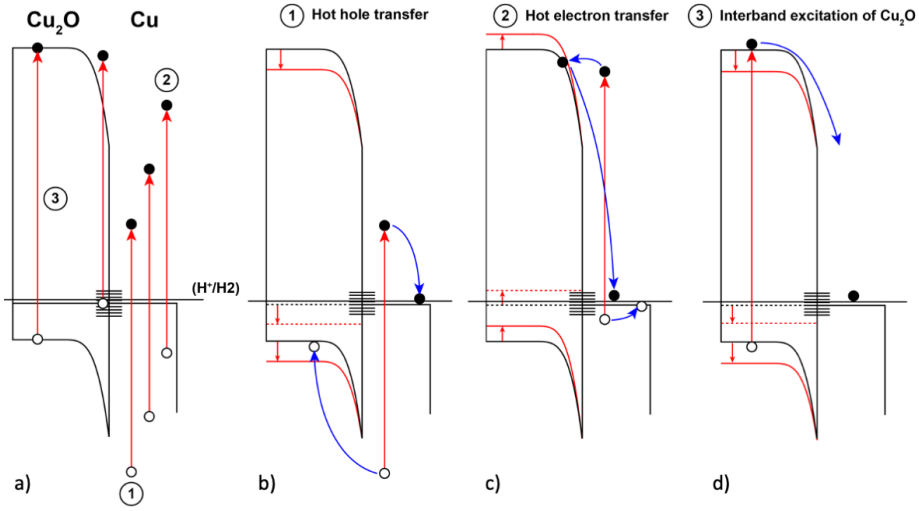

Figure 6. Band alignment of the plasma-treated Cu_2O-Cu NCs heterostructure with a) relevant optical processes illustrated. The heights of the tunneling barriers, optical excitation, and band-gaps are scaled accurately to one another. Empty (filled) circles indicate photo-excited holes (electrons). The band levels are also shown accurately with respect to the reversible hydrogen electrode potential. Proposed b) hot hole transfer; c) hot electron transfer and d) interband excitation processes.

In the Cu_2O-Cu NCs heterostructure, the following photo-physical mechanisms play a role during the timescales probed by ultrafast TA spectroscopy: hot hole/electron transfer due to optical excitation of the Cu NC LSPR (Fig. 6b,c); electron transfer from Cu_2O to Cu due to direct interband excitation (Fig. 6d); and near-field enhanced surface/interfacial state excitation. These mechanisms manifest changes in the optical properties of Cu_2O bulk, Cu NCs, and the junction itself, via charge

accumulation across the junction which changes the tunneling barrier; and changes in electron density of the Cu NCs, which shifts the Cu NCs LSPR.

Two optical pump energies are considered: 3.1 eV (interband) and 2.0 eV (intraband, in resonance with the Cu LSPR). Consider first excitation of the Cu LSPR: in the case of intraband excitation, the optical absorption is strongly enhanced by the LSPR relative to the bulk absorption of Cu. In the case of interband excitation, the optical absorption is only weakly enhanced since the excitation is off resonance with the LSPR. Intraband excitation of the Cu NCs drives changes in both the electron and hole populations over an energy range $E_{Fermi} \pm E_{pump}$. Immediately after optical excitation and earlier than 100 fs, this distribution is highly non-thermal[75–78] and also depends on the density of states of Cu[79,80]. The holes generated in Cu deeper than the tunneling barrier (1.1 eV deep) can easily tunnel, whereas the electrons remain trapped in the Cu NCs. This tunneling is still possible after hot Fermi gas formation, but thermal hole/electron distributions form within a few 100 fs due to Landau damping[76] and only the tails of the distributions are energetically allowed to tunnel. In this case of hole tunneling from Cu to Cu_2O, the Cu NC electron density increases along with the plasma frequency, therefore causing a blue-shift of the LSPR[81,82], as observed in the TA experiments (Fig. 6d,f). In the case of electron tunneling, the barrier from Cu to Cu_2O is 1.3 eV, but the difference in energy between the CB of Cu_2O and Fermi level far from the junction is 2.1 eV. Thus, hot electrons may diffuse from Cu into Cu_2O, but are thermodynamically favored to relax downhill to Cu, and thus do not contribute to the observed TA signal. Another effect that is relevant due to the presence of the Cu LSPR is near-field enhancement of excitation of surface/interfacial states at the Cu_2O/Cu NCs junction. It is well-understood that plasmonic NCs strongly enhance the near-field within a few nanometers of the NC surface, especially at the resonance energy of the LSPR[83]. The presence of surface/interfacial states and vacancies has been reported in copper oxide, and likely manifests in optical measurements as an Urbach tail[60,61]. We noticed the PIA signals on the red side of the Cu_2O band-edge, in both the pristine and plasma-treated Cu_2O samples (Fig. 6d,e), but do not go into further detail on this mechanism.

When excitation of Cu_2O bulk is considered, only the interband excitation mechanism is relevant. Electrons are promoted to the CB and a hole is left behind in the VB. The photo-electron drifts across the junction due to the in-built field (Figure 6d) and is eventually trapped in the Cu NCs, where it can participate in HER; holes are prevented from drifting into the Cu NCs by the tunneling barrier. Thus, the result is the same as intraband excitation of the Cu LSPR: holes accumulate in Cu_2O and electrons in Cu (further details on charge transfer processes, studied with ultrafast differential transmission, are discussed in the Supplementary Discussion).

In summary, optical excitation of both the Cu NCs and Cu_2O bulk leads to separation of holes and electrons across the junction, with electrons accumulating in the Cu NCs and holes in the Cu_2O bulk. The effect of this charge accumulation is an overall reduction in the hole tunneling barrier from Cu_2O to Cu, since the Cu_2O bulk becomes more positively charged (Fig. 6b). The extreme result of continuous hole transfer under optical excitation is the eventual reversal of the carrier tunneling barrier from a hole barrier to an electron barrier in the CB, at which point optical excitation no longer leads to an accumulation of electrons in Cu. This phenomenon may have important consequences on sample degradation under ambient conditions, as well as on the efficiency of the HER process in a PEC cell. In particular, it may be the cause of the delayed degradation that we observe in the plasma-treated Cu_2O thin films under *operando* conditions: the lower amounts of electrons accumulating in the Cu seeds and then in progressively formed Cu NCs, compared to the case of the pristine Cu_2O sample, hinders the formation of the thick and compact metallic layer, which covers the surface of the latter after PEC. Taking into consideration this phenomenon, clarified through the previous advanced optical analysis, we can actually explain the higher current density that is delivered by the pristine sample with respect to the plasma-modified one, within the

first 200 s of PEC HER (Fig. 1a). Indeed, in the former sample, a major quantity of electrons reaches the junction, making HER immediately more efficient, while in the latter the delaying reserve mechanism hinders the electron flux towards water molecules, and this results in a lower current at the electrode. Since anyway the high initial rate of electron accumulation on the surface at the beginning of the process is also the cause of the fast degradation of the pristine Cu_2O photocathode, after around 200 s this sample starts to under-perform with respect to the plasma-treated one. This last one, while having a slower initial kinetic, can still keep on delivering an efficient HER over longer times: in this sense, we argue that the complex plasmon-assisted phenomena happening at the Cu_2O/Cu NCs junction is a sort of *operando* "self-healing" mechanism, which has been integrated in the plasma-treated photocathode and preserves its stability during PEC HER.

Conclusion

In this work, we present the effect of an argon-plasma surface treatment on a Cu_2O photocathode, finding an improved stability in PEC HER with respect to the reference un-treated electrode. We further identify the reason for this stabilization in the formation, during the hydrogen evolution process, of plasmonic copper metal-based hierarchical nanostructures, differently from the case of pristine Cu_2O, onto which only a compact copper layer is formed, ultimately blocking the photoreaction. The plasmonic character of these nanostructures contributes to establish a complex photophysical mechanism within the resulting Cu_2O/Cu heterostructure, that delays the degradation and thus allows for the measured longer shelf-life of the photocathode. While in the reference case, electrons are only transferred from Cu_2O to the surface to generate non-structured metallic copper that irreversibly covers the photocathode and dramatically jeopardizes the PEC performance, in the plasmonic-enriched electrode, a virtuous balance between Cu_2O dissolution and Cu oxidation is established, which resembles a net *operando* self-healing.

Our findings provide a new technological strategy to improve the functionality of non-critical energy-related raw materials, which will serve to better exploit our domestic and abundant resources for the future sustainable production of clean energy.

Acknowledgments

We thank Miss Xiaoying Zhu and Dr. Mengjiao Wang for help with graphics. We also thank Dr. Andrea Basagni for SEM-EDX analyses and Mr Pietro Dalle Feste for help with sample preparation.

Funding: D.R.-M., R.M., F.S. and T.G. acknowledge financial support from the European Commission through H2020 FET-PROACTIVE-EIC-07-2020 project LIGHT-CAP (project number 101017821). S.G. acknowledges financial support from DFG CRC 1441 project Track-Act.

Author Contribution

Conceptualization: F.L. and T.G. Methodology: A.M.R., G.A.R., A.P., F.S., T.G. and F.L. Validation: A.M.R., G.A.R., F.C. Investigation: A.M.R., F.C., A.P., D.R.M, R.M., M.S., F.Sch., E.N., S.M. and M.P. Visualization: A.M.R. and F.L. Writing (original draft): A.M.R., F.S., T.G. and F.L. Writing (editing and review): All authors.

Competing interests: The authors declare that they have no competing interests.

Data and materials availability: All data needed to evaluate the conclusions in the paper are present in the paper and/or the Supporting Information. All data can be accessed at the repository.

Supporting Information

This PDF file includes:

Supplementary Discussion
Fig. S1 to S7
Table S1 and S2
References

References

[1] T. Baran, A. Visibile, M. Busch, X. He, S. Wojtyla, S. Rondinini, A. Minguzzi, A. Vertova, *Molecules* **2021**, *26*, 7271.
[2] Y. J. Jang, J. S. Lee, *ChemSusChem* **2019**, *12*, 1835.
[3] Y. Yang, D. Xu, Q. Wu, P. Diao, *Sci. Rep.* **2016**, *6*, 35158.
[4] T. Gatti, F. Lamberti, R. Mazzaro, I. Kriegel, D. Schlettwein, F. Enrichi, N. Lago, E. Di Maria, G. Meneghesso, A. Vomiero, S. Gross, *Adv. Energy Mater.* **2021**, *11*, 2101041.
[5] J. Arem, *Color Encyclopedia of Gemstones* (Ed.: Nostrand Reinhold Company, Van), **1977**.
[6] K. J. J. Kuipers, L. F. C. M. van Oers, M. Verboon, E. van der Voet, *Glob. Environ. Chang.* **2018**, *49*, 106.
[7] A. Paracchino, V. Laporte, K. Sivula, M. Grätzel, E. Thimsen, *Nat. Mater.* **2011**, *10*, 456.
[8] L. Pan, J. H. Kim, M. T. Mayer, M.-K. Son, A. Ummadisingu, J. S. Lee, A. Hagfeldt, J. Luo, M. Grätzel, *Nat. Catal.* **2018**, *1*, 412.
[9] A. Zaitsev, A. Lacoste, F. Poncin-Epaillard, A. Bès, D. Debarnot, *Surf. Coatings Technol.* **2017**, *330*, 196.
[10] S. P. Zimin, E. S. Gorlachev, D. A. Mokrov, I. I. Amirov, V. V Naumov, V. F. Gremenok, R. Juskenas, M. Skapas, W. Y. Kim, K. Bente, Y.-D. Chung, *Semicond. Sci. Technol.* **2017**, *32*, 075014.
[11] S. P. Zimin, N. N. Kolesnikov, I. I. Amirov, V. V. Naumov, E. S. Gorlachev, S. Kim, N.-H. Kim, *Crystals* **2022**, *12*, 111.
[12] S. Li, T. Guo, Y. Li, S. Yun, H. Xu, H. Li, A. Huang, *Mater. Res. Bull.* **2022**, *147*, 111666.
[13] S. V. Boriskina, H. Ghasemi, G. Chen, *Mater. Today* **2013**, *16*, 375.
[14] P. V. Kamat, G. V. Hartland, *ACS Energy Lett.* **2018**, *3*, 1467.
[15] R. F. Hamans, R. Kamarudheen, A. Baldi, *Nanomaterials* **2020**, *10*, 2377.
[16] E. Cortés, L. V. Besteiro, A. Alabastri, A. Baldi, G. Tagliabue, A. Demetriadou, P. Narang, *ACS Nano* **2020**, *14*, 16202.
[17] P. Subramanyam, B. Meena, V. Biju, H. Misawa, S. Challapalli, *J. Photochem. Photobiol. C Photochem. Rev.* **2022**, *51*, 100472.
[18] Y. Zhang, W. Guo, Y. Zhang, W. D. Wei, *Adv. Mater.* **2021**, *33*, 2006654.
[19] J. C. Alexander, *Surface Modifications and Growth of Titanium Dioxide for Photo-Electrochemical Water Splitting*, Springer International Publishing, Cham, **2016**.
[20] J. Cai, J. Shen, X. Zhang, Y. H. Ng, J. Huang, W. Guo, C. Lin, Y. Lai, *Small Methods* **2019**, *3*, 1800184.
[21] M. Glaeske, S. Juergensen, L. Gabrielli, E. Menna, F. Mancin, T. Gatti, A. Setaro, *Phys. status solidi – Rapid Res. Lett.* **2018**, *12*, 1800508.
[22] N. Pariona, S. Basurto Cereceda, F. Mondaca, G. Carrión, A. I. Mtz-Enriquez, *Mater. Lett.* **2021**, *301*, 130182.
[23] D. Jiang, Y. Zhang, X. Li, *Chinese J. Catal.* **2019**, *40*, 105.
[24] W.-Q. Xu, S. He, C.-C. Lin, X.-J. Liu, L.-C. Jiang, J.-J. Jiang, *Chinese J. Struct. Chem.* **2020**, *39*, 1522.
[25] N. Farahbakhsh, S. Sanjabi, *J. Ind. Eng. Chem.* **2019**, *70*, 211.

Codice campo modificato

Formattato: Inglese americano

Formattato: Inglese americano

Formattato: Inglese americano

Formattato: Inglese americano

[26] M. Sayed, J. Yu, G. Liu, M. Jaroniec, *Chem. Rev.* **2022**, *122*, 10484.
[27] M. Sayed, L. Zhang, J. Yu, *Chem. Eng. J.* **2020**, *397*, 125390.
[28] K. Shantha Seelan, K. Ravichandran, P. Kavitha, P. K. Praseetha, *Appl. Phys. A* **2020**, *126*, 750.
[29] K. Sugawa, N. Tsunenari, H. Takeda, S. Fujiwara, T. Akiyama, J. Honda, S. Igari, W. Inoue, K. Tokuda, N. Takeshima, Y. Watanuki, S. Tsukahara, K. Takase, T. Umegaki, Y. Kojima, N. Nishimiya, N. Fukuda, Y. Kusaka, H. Ushijima, J. Otsuki, *Langmuir* **2017**, *33*, 5685.
[30] Y. Cheng, Y. Lin, J. Xu, J. He, T. Wang, G. Yu, D. Shao, W.-H. Wang, F. Lu, L. Li, X. Du, W. Wang, H. Liu, R. Zheng, *Appl. Surf. Sci.* **2016**, *366*, 120.
[31] F. Hu, Y. Zou, L. Wang, Y. Wen, Y. Xiong, *Int. J. Hydrogen Energy* **2016**, *41*, 15172.
[32] T. D. Golden, M. G. Shumsky, Y. Zhou, R. A. VanderWerf, R. A. Van Leeuwen, J. A. Switzer, *Chem. Mater.* **1996**, *8*, 2499.
[33] J. I. Goldstein, D. E. Newbury, J. R. Michael, N. W. M. Ritchie, J. H. J. Scott, D. C. Joy, *Scanning Electron Microscopy and X-Ray Microanalysis*, Springer New York, New York, NY, **2018**.
[34] I. V. Bagal, N. R. Chodankar, M. A. Hassan, A. Waseem, M. A. Johar, D. H. Kim, S. W. Ryu, *Int. J. Hydrogen Energy* **2019**, *44*, 21351.
[35] P. Marathey, B. Patel, S. Khanna, A. Vanpariya, A. Ray, *Int. J. Hydrogen Energy* **2021**, *46*, 16431.
[36] Z. Shengsen, Y. Jie, Y. Siyuan, X. Yuehua, C. Xin, L. Xin, Z. Xiangchao, P. Feng, F. Yueping, *Chin. J. Catal.* **2017**, *38*, 365.
[37] P. P. Kunturu, J. Huskens, *ACS Appl. Energy Mater.* **2019**, *2*, 7850.
[38] Y. Sawada, H. Tamaru, M. Kogoma, M. Kawase, K. Hashimoto, *J. Phys. D. Appl. Phys.* **1996**, *29*, 2539.
[39] H. Inui, K. Takeda, H. Kondo, K. Ishikawa, M. Sekine, H. Kano, N. Yoshida, M. Hori, *Appl. Phys. Express* **2010**, *3*, 126101.
[40] J. Y. Kim, J. A. Rodriguez, J. C. Hanson, A. I. Frenkel, P. L. Lee, *J. Am. Chem. Soc.* **2003**, *125*, 10684.
[41] O. Schalm, A. Patelli, P. Storme, A. Crabbé, S. Voltolina, V. Feyer, H. Terryn, *Corros. Sci.* **2021**, *178*, 109074.
[42] S. Tajima, S. Tsuchiya, M. Matsumori, S. Nakatsuka, T. Ichiki, *Trans. Mater. Res. Soc. Japan* **2010**, *35*, 621.
[43] A. Paracchino, J. C. Brauer, J.-E. Moser, E. Thimsen, M. Graetzel, *J. Phys. Chem. C* **2012**, *116*, 7341.
[44] J. Liu, J. Li, K.-J. Mu, X.-W. Shi, J.-Q. Wang, M. Mao, S. Chen, E.-J. Liang, *Chinese Phys. B* **2021**, *30*, 114205.
[45] Q. Huang, F. Kang, H. Liu, Q. Li, X. Xiao, *J. Mater. Chem. A* **2013**, *1*, 2418.
[46] P. Basnet, Metal oxide photocatalytic nanostructures fabricated by dynamic shadowing growth, University of Georgia, **2015**.
[47] Q. Zhang, K. Zhang, D. Xu, G. Yang, H. Huang, F. Nie, C. Liu, S. Yang, *Prog. Mater. Sci.* **2014**, *60*, 208.
[48] B. K. Meyer, A. Polity, D. Reppin, M. Becker, P. Hering, P. J. Klar, T. Sander, C. Reindl, J. Benz, M. Eickhoff, C. Heiliger, M. Heinemann, J. Bläsing, A. Krost, S. Shokovets, C. Müller, C. Ronning, *Phys. status solidi* **2012**, *249*, 1487.
[49] A. S. Zoolfakar, R. A. Rani, A. J. Morfa, A. P. O'Mullane, K. Kalantar-zadeh, *J. Mater. Chem. C* **2014**, *2*, 5247.
[50] C. Malerba, F. Biccari, C. Leonor Azanza Ricardo, M. D'Incau, P. Scardi, A. Mittiga, *Sol. Energy Mater. Sol. Cells* **2011**, *95*, 2848.

Formattato: Inglese americano

Formattato: Inglese americano

[51] S. T. Omelchenko, Y. Tolstova, H. A. Atwater, N. S. Lewis, *ACS Energy Lett.* **2017**, *2*, 431.
[52] I. Pastoriza-Santos, A. Sánchez-Iglesias, B. Rodríguez-González, L. M. Liz-Marzán, *Small* **2009**, *5*, 440.
[53] C. Lee, Y. Park, J. Y. Park, *RSC Adv.* **2019**, *9*, 18371.
[54] M. Tariq, M. D. Koch, J. W. Andrews, K. E. Knowles, *J. Phys. Chem. C* **2020**, *124*, 4810.
[55] P. Liu, H. Wang, X. Li, M. Rui, H. Zeng, *RSC Adv.* **2015**, *5*, 79738.
[56] H. Wang, F. Tam, N. K. Grady, N. J. Halas, *J. Phys. Chem. B* **2005**, *109*, 18218.
[57] J. L. Duan, T. W. Cornelius, J. Liu, S. Karim, H. J. Yao, O. Picht, M. Rauber, S. Müller, R. Neumann, *J. Phys. Chem. C* **2009**, *113*, 13583.
[58] F. Scotognella, G. Della Valle, A. R. Srimath Kandada, D. Dorfs, M. Zavelani-Rossi, M. Conforti, K. Miszta, A. Comin, K. Korobchevskaya, G. Lanzani, L. Manna, F. Tassone, *Nano Lett.* **2011**, *11*, 4711.
[59] M. Zavelani-Rossi, D. Polli, S. Kochtcheev, A.-L. Baudrion, J. Béal, V. Kumar, E. Molotokaite, M. Marangoni, S. Longhi, G. Cerullo, P.-M. Adam, G. Della Valle, *ACS Photonics* **2015**, *2*, 521.
[60] F. Urbach, *Phys. Rev.* **1953**, *92*, 1324.
[61] H. Tang, F. Lévy, H. Berger, P. E. Schmid, *Phys. Rev. B* **1995**, *52*, 7771.
[62] J.-Y. Bigot, V. Halté, J.-C. Merle, A. Daunois, *Chem. Phys.* **2000**, *251*, 181.
[63] I. H. M. van Stokkum, D. S. Larsen, R. van Grondelle, *Biochim. Biophys. Acta - Bioenerg.* **2004**, *1657*, 82.
[64] L. Jiang, H.-L. Tsai, *J. Heat Transfer* **2005**, *127*, 1167.
[65] K.-S. Lee, M. A. El-Sayed, *J. Phys. Chem. B* **2006**, *110*, 19220.
[66] E. Petryayeva, U. J. Krull, *Anal. Chim. Acta* **2011**, *706*, 8.
[67] F. Scotognella, G. Della Valle, A. R. Srimath Kandada, M. Zavelani-Rossi, S. Longhi, G. Lanzani, F. Tassone, *Eur. Phys. J. B* **2013**, *86*, 154.
[68] K. Wu, J. Chen, J. R. McBride, T. Lian, *Science (80-.).* **2015**, *349*, 632.
[69] W. Li, J. G. Valentine, *Nanophotonics* **2017**, *6*, 177.
[70] F. V. A. Camargo, Y. Ben-Shahar, T. Nagahara, Y. E. Panfil, M. Russo, U. Banin, G. Cerullo, *Nano Lett.* **2021**, *21*, 1461.
[71] M. Ahlawat, D. Mittal, V. Govind Rao, *Commun. Mater.* **2021**, *2*, 114.
[72] P. A. Anderson, *Phys. Rev.* **1949**, *76*, 388.
[73] R. E. Brandt, M. Young, H. H. Park, A. Dameron, D. Chua, Y. S. Lee, G. Teeter, R. G. Gordon, T. Buonassisi, *Appl. Phys. Lett.* **2014**, *105*, 263901.
[74] S. Trasatti, *Pure Appl. Chem.* **1986**, *58*, 955.
[75] G. V. Hartland, *Chem. Rev.* **2011**, *111*, 3858.
[76] Y. Zhang, S. He, W. Guo, Y. Hu, J. Huang, J. R. Mulcahy, W. D. Wei, *Chem. Rev.* **2018**, *118*, 2927.
[77] T. Heilpern, M. Manjare, A. O. Govorov, G. P. Wiederrecht, S. K. Gray, H. Harutyunyan, *Nat. Commun.* **2018**, *9*, 1853.
[78] L. Chang, L. V. Besteiro, J. Sun, E. Y. Santiago, S. K. Gray, Z. Wang, A. O. Govorov, *ACS Energy Lett.* **2019**, *4*, 2552.
[79] G. Della Valle, F. Scotognella, A. R. S. Kandada, M. Zavelani-Rossi, H. Li, M. Conforti, S. Longhi, L. Manna, G. Lanzani, F. Tassone, *J. Phys. Chem. Lett.* **2013**, *4*, 3337.
[80] S. Hüfner, G. K. Wertheim, N. V. Smith, M. M. Traum, *Solid State Commun.* **1972**, *11*, 323.
[81] I. Kriegel, C. Urso, D. Viola, L. De Trizio, F. Scotognella, G. Cerullo, L. Manna, *J. Phys. Chem. Lett.* **2016**, *7*, 3873.
[82] M. Ghini, N. Curreli, A. Camellini, M. Wang, A. Asaithambi, I. Kriegel, *Nanoscale* **2021**, *13*, 8773.
[83] V. Amendola, R. Pilot, M. Frasconi, O. M. Maragò, M. A. Iatì, *J. Phys. Condens. Matter* **2017**,

29, 203002.